1 Molecular Dynamics Simulations of Granular Materials

Summary

One challenge of todays research is the realistic simulation of granular materials consisting of millions of particles. In this chapter, the molecular dynamics method for the simulation of many-particle systems is briefly introduced and some examples of applications are presented.

There exist two basically different approaches, the so-called soft particle molecular dynamics and the hard sphere, event-driven method. The former is straightforward, easy to generalize, and has numberless applications, while the latter is optimized for rigid interactions and is mainly used for collisional, dissipative granular gases.

The examples given include homogeneous and clustering granular gases, and bi-axial or cylindrical compression/shearing of dense packings.

Keywords

granular matter, molecular dynamics (MD), event driven MD, parallelization, equation of state, clustering, shear-cell, shear band formation

1.1 Introduction

A straightforward approach towards the understanding of macroscopic material behavior by just modeling and simulating all atoms in a macroscopic system is not possible due to the huge number of degrees of freedom. Therefore, one could reduce the size of the system under consideration, so that a microscopic simulation of atoms is possible. However, the possible length of such a "probe" is in general too small in order to regard it as macroscopic. Therefore, methods and tools to perform a so-called micro-macro transition [1–3] are discussed in this study, starting from the molecular dynamics simulations. These "microscopic" simulations of a small sample (representative volume element) are used to derive macroscopic constitutive relations needed to describe the material within the framework of a macroscopic continuum theory.

For granular materials, as an example, the particle properties and interaction laws are inserted into a discrete particle molecular dynamics (MD) and lead to the collective behavior of the dissipative many-particle system. From the particle simulation, one can extract, e.g., the pressure of the system as a function of density. This equation of state allows a macroscopic description of the material, which can be viewed as a compressible, non-Newtonian complex fluid [4], including a fluid-solid phase transition.

In the following, two versions of the molecular dynamics simulation method are introduced. The first is the so-called soft sphere molecular dynamics (MD), as described in section 1.2. It is a straightforward implementation to solve the equations of motion for a system of many interacting particles [5, 6]. For MD, both normal and tangential interactions, like friction, are discussed for spherical particles. The second method is the so-called event-driven (ED) simulation, as discussed in section 1.3, which is conceptually different from MD, since collisions are dealt with via a collision matrix that determines the momentum change on physical grounds. For the sake of brevity, the ED method is only discussed for smooth spherical particles. A comparison and a way to switch between the soft and hard particle methods is provided in section 1.4.

As one ingredient of a micro-macro transition, the stress is defined for a dynamic system of hard spheres, in section 1.5, by means of kinetic-theory arguments [2], and for a quasi-static system by means of volume averages [7]. Examples are presented in the following sections 1.6 and 1.7, where the above-described methods are applied.

1.2 The Soft Particle Molecular Dynamics Method

One possibility to obtain information about the behavior of granular media is to perform experiments. An alternative are simulations with the molecular dynamics (MD) or discrete element model (DEM) [1, 8–15]. Note that both methods are identical in spirit, however, different groups of researchers use these (and also other) names.

Conceptually, the MD or DEM method has to be separated from the hard sphere event-driven (ED) molecular dynamics, see section 1.3, and also from the so-called Contact Dynamics (CD). The former will be discussed below, the latter (CD) will be introduced in the chapter by D. Wolf in this book [**?**]. Alternative methods like cell-models or lattice gas methods are not discussed here at all.

1.2.1 Discrete Particle Model

The elementary units of granular materials are mesoscopic grains which deform under stress. Since the realistic modeling of the deformations of the particles is much too complicated, we relate the interaction force to the overlap δ of two particles, see Fig. 1.1. Note that the evaluation of the inter-particle forces based on the overlap may not be sufficient to account for the inhomogeneous stress distribution inside the particles. Consequently, our results presented below are of the same quality as the simple assumptions about the force-overlap relation, see Fig. 1.1.

1.2.2 Equations of Motion

If all forces $\boldsymbol{f}_i$ acting on the particle i, either from other particles, from boundaries or from external forces, are known, the problem is reduced to the integration of Newton's equations of motion for the translational and rotational degrees of freedom:

$$m_i \frac{\mathrm{d}^2}{\mathrm{d}t^2}\boldsymbol{r}_i = \boldsymbol{f}_i + m_i \boldsymbol{g} \;, \quad \text{and} \quad I_i \frac{\mathrm{d}^2}{\mathrm{d}t^2}\boldsymbol{\varphi}_i = \boldsymbol{t}_i \tag{1.1}$$

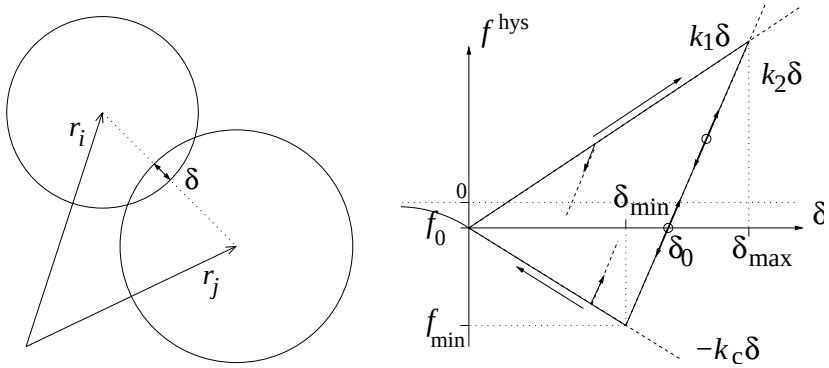

Figure 1.1: (Left) Two particle contact with overlap δ. (Right) Schematic graph of the piecewise linear, hysteretic, cohesive force-displacement model used below.

with the mass m_i of particle i, its position $\boldsymbol{r}_i$ the total force $\boldsymbol{f}_i = \sum_c \boldsymbol{f}_i^c$ acting on it due to contacts with other particles or with the walls, the acceleration due to volume forces like gravity $\boldsymbol{g}$, the spherical particles moment of inertia I_i, its angular velocity $\boldsymbol{\omega}_i = \mathrm{d}\boldsymbol{\varphi}_i/\mathrm{d}t$ and the total torque $\boldsymbol{t}_i = \sum_c \boldsymbol{l}_i^c \times \boldsymbol{f}_i^c$.

The equations of motion are thus a system of $\mathcal{D}+\mathcal{D}(\mathcal{D}-1)/2$ coupled ordinary differential equations to be solved in $\mathcal{D}$ dimensions. With tools from numerical integration, as nicely described in textbooks as [5, 6], this is straightforward. The typically short-ranged interactions in granular media, allow for a further optimization by using linked-cell or alternative methods [5, 6] in order to make the neighborhood search more efficient. In the case of long-range interactions, (e.g. charged particles with Coulomb interaction, or objects in space with self-gravity) this is not possible anymore, so that more advanced methods for optimization have to be applied – for the sake of brevity, we restrict ourselves to short range interactions here.

1.2.3 Contact Force Laws

Linear Normal Contact Model

Two spherical particles i and j, with radii a_i and a_j, respectively, interact only if they are in contact so that their overlap

$$\delta = (a_i + a_j) - (\boldsymbol{r}_i - \boldsymbol{r}_j) \cdot \boldsymbol{n} \tag{1.2}$$

is positive, $\delta > 0$, with the unit vector $\boldsymbol{n} = \boldsymbol{n}_{ij} = (\boldsymbol{r}_i - \boldsymbol{r}_j)/|\boldsymbol{r}_i - \boldsymbol{r}_j|$ pointing from j to i. The force on particle i, from particle j, at contact c, can be decomposed into a normal and a tangential part as $\boldsymbol{f}^c := \boldsymbol{f}_i^c = f^n\boldsymbol{n} + f^t\boldsymbol{t}$, where f^n is discussed first.

The simplest normal contact force model, which takes into account excluded volume and dissipation, involves a linear repulsive and a linear dissipative force

$$f^n = k\delta + \gamma_0 v_n \,, \tag{1.3}$$

with a spring stiffness k, a viscous damping γ_0, and the relative velocity in normal direction $v_n = -\boldsymbol{v}_{ij} \cdot \boldsymbol{n} = -(\boldsymbol{v}_i - \boldsymbol{v}_j) \cdot \boldsymbol{n} = \dot{\delta}$.

This so-called linear spring dashpot model allows to view the particle contact as a damped harmonic oscillator, for which the half-period of a vibration around an equilibrium position, see Fig. 1.1, can be computed, and one obtains a typical response time on the contact level,

$$t_c = \frac{\pi}{\omega} \,, \quad \text{with} \quad \omega = \sqrt{(k/m_{12}) - \eta_0^2} \,, \tag{1.4}$$

with the eigenfrequency of the contact ω, the rescaled damping coefficient $\eta_0 = \gamma_0/(2m_{ij})$, and the reduced mass $m_{ij} = m_i m_j/(m_i + m_j)$. From the solution of the equation of a half period of the oscillation, one also obtains the coefficient of restitution

$$r = v_n'/v_n = \exp\left(-\pi\eta_0/\omega\right) = \exp\left(-\eta_0 t_c\right) \,, \tag{1.5}$$

which quantifies the ratio of relative velocities after (primed) and before (unprimed) the collision. For a more detailed discussion of this and other, more realistic, non-linear contact models see e.g. [16] and the chapters by Pöschel and Wolf in this book [**?**, **?**].

The contact duration in Eq. (1.4) is also of practical technical importance, since the integration of the equations of motion is stable only if the integration time-step Δt_{MD} is much smaller than t_c. Furthermore, it depends on the magnitude of dissipation. In the extreme case of an overdamped spring, t_c can become very large. Therefore, the use of neither too weak nor too strong dissipation is recommended.

Cohesive Normal Contact Model

Here we apply a variant of the linear hysteretic spring model [16–18], as an alternative to the frequently applied spring-dashpot models. This model is the simplest version of some more complicated nonlinear-hysteretic force laws [17, 19, 20], which reflect the fact that at the contact point, plastic deformations may take place. The repulsive (hysteretic) force can be written as

$$f^{\mathrm{hys}} = \begin{cases} k_1\delta & \text{for loading,} & \text{if } k_2(\delta - \delta_0) \geq k_1\delta \\ k_2(\delta - \delta_0) & \text{for un/reloading,} & \text{if } k_1\delta > k_2(\delta - \delta_0) > -k_c\delta \\ -k_c\delta & \text{for unloading,} & \text{if } -k_c\delta \geq k_2(\delta - \delta_0) \end{cases} \tag{1.6}$$

with $k_1 \leq k_2$, see Fig. 1.1.

During the initial loading the force increases linearly with the overlap δ, until the maximum overlap $\delta_{\max}$ is reached (which has to be kept in memory as a history parameter). The line with slope k_1 thus defines the maximum force possible for a given δ. During unloading the force drops from its value at $\delta_{\max}$ down to zero at overlap $\delta_0 = (1 - k_1/k_2)\delta_{\max}$, on the line with slope k_2. Reloading at any instant leads to an increase of the force along this line, until the maximum force is reached; for still increasing δ, the force follows again the line with slope k_1 and $\delta_{\max}$ has to be adjusted accordingly.

Unloading below δ_0 leads to negative, attractive forces until the minimum force $-k_c\delta_{\min}$ is reached at the overlap $\delta_{\min} = (k_2 - k_1)\delta_{\max}/(k_2 + k_c)$. This minimum force, i.e. the maximum attractive force, is obtained as a function of the model parameters k_1, k_2, k_c, and

the history parameter $\delta_{\max}$. Further unloading leads to attractive forces $f^{\rm hys} = -k_c\delta$ on the cohesive branch with slope $-k_c$. The highest possible attractive force, for given k_1 and k_2, is reached for $k_c \to \infty$, so that $f^{\rm hys}_{\max} = -(k_2 - k_1)\delta_{\max}$. Since this would lead to a discontinuity at $\delta = 0$, it is avoided by using finite k_c.

The lines with slope k_1 and $-k_c$ define the range of possible force values and departure from these lines takes place in the case of unloading and reloading, respectively. Between these two extremes, unloading and reloading follow the same line with slope k_2. Possible equilibrium states are indicated as circles in Fig. 1.1, where the upper and lower circle correspond to a pre-stressed and stress-free state, respectively. Small perturbations lead, in general, to small deviations along the line with slope k_2 as indicated by the arrows.

A non-linear un/reloading behavior would be more realistic, however, due to a lack of detailed experimental informations, we use the piece-wise linear model as a compromise. One refinement is a k_2 value dependent on the maximum overlap that implies small and large plastic deformations for weak and strong contact forces, respectively. One model, as implemented recently [21], requires an additional model parameter, $\delta^*_{\max}$, so that $k_2(\delta_{\max})$ is increasing from k_1 to k_2 (linear interpolation) with the maximum overlap, until $\delta^*_{\max}$ is reached [1]:

$$k_2(\delta_{\max}) = \begin{cases} k_2 & \text{if } \delta_{\max} \geq \delta^*_{\max} \\ k_1 + (k_2 - k_1)\delta_{\max}/\delta^*_{\max} & \text{if } \delta_{\max} < \delta^*_{\max} \end{cases} . \tag{1.7}$$

While in the case of collisions of particles with large deformations, dissipation takes place due to the hysteretic nature of the force-law, stronger dissipation of small amplitude deformations is achieved by adding the viscous, velocity dependent dissipative force from Eq. (1.3) to the hysteretic force, such that $f^n = f^{\rm hys} + \gamma_0 v_n$. The hysteretic model contains the linear contact model as special case $k_1 = k_2 = k$.

Tangential Contact Model

The force in tangential direction is implemented in the spirit of Cundall and Strack [8], who introduced a tangential spring in order to account for static friction. Various authors have used this idea and numerous variants were implemented, see [22] for a summary and discussion.

Since we use a formulation which is generalized to dimensions $\mathcal{D} = 2$ and $\mathcal{D} = 3$, and which also takes into account static and dynamic friction coefficients, it is necessary to repeat the model and define the details of the implementation. Note however, that we only discuss sliding/sticking friction and disregard rolling [23] and torsion friction [**?**] here.

The tangential force is coupled to the normal force via Coulombs law, i.e. $f^t \leq \mu^s f^n$, where for the limit case one has dynamic friction with $f^t = \mu^d f^n$. The dynamic and the static friction coefficients follow, in general, the relation $\mu^d \leq \mu^s$. The static situation requires an elastic spring in order to allow for a restoring force, i.e. a non-zero remaining tangential force in static equilibrium due to activated Coulomb friction.

If a repulsive contact is established, and thus one has $f^n > 0$, the tangential force is active. In the presence of cohesion, Coulombs law has to be slightly modified in so far that f^n is replaced by $f^n + k_c\delta$. With other words, the reference criterion for a contact is no longer the zero force level, but it is the cohesive, attractive force level along $-k_c\delta$.

[1] A limit to the slope k_2 is needed for practical reasons. If k_2 would not be limited, the contact duration could become very small so that the time step would have to be reduced below reasonable values.

If a contact is active, we project the tangential spring into the actual tangential plane [2]

$$\boldsymbol{\xi} = \boldsymbol{\xi}' - \boldsymbol{n}(\boldsymbol{n} \cdot \boldsymbol{\xi}') \;, \tag{1.8}$$

where $\boldsymbol{\xi}'$ is the old spring from the last iteration. This action is relevant only for an already existing spring; if the spring is new, the tangential spring-length is zero anyway, however, its change is well defined even for the first, initiation step. The tangential velocity, as needed in the following, is

$$\boldsymbol{v}_t = \boldsymbol{v}_{ij} - \boldsymbol{n}(\boldsymbol{n} \cdot \boldsymbol{v}_{ij}) \;, \tag{1.9}$$

with the total relative velocity of the particle surfaces at the contact

$$\boldsymbol{v}_{ij} = \boldsymbol{v}_i - \boldsymbol{v}_j + a_i \boldsymbol{n} \times \boldsymbol{\omega}_i + a_j \boldsymbol{n} \times \boldsymbol{\omega}_j \;. \tag{1.10}$$

In order to compute the changes of the tangential spring, we first compute the tangential test-force as the sum of the tangential spring and a tangential viscous force (in analogy to the normal viscous force)

$$\boldsymbol{f}_{\mathrm{o}}^t = -k_t \boldsymbol{\xi} - \gamma_t \boldsymbol{v}_t \;, \tag{1.11}$$

with the tangential spring stiffness k_t and the tangential dissipation parameter γ_t. As long as $|\boldsymbol{f}_{\mathrm{o}}^t| \leq f_C^s$, with $f_C^s = \mu^s(f^n + k_c\delta)$, one has static friction and, on the other hand, if the limit $|\boldsymbol{f}_{\mathrm{o}}^t| > f_C^s$ is reached, sliding friction is active with magnitude $f_C^d = \mu^d(f^n + k_c\delta)$. (As soon as $|\boldsymbol{f}_{\mathrm{o}}^t|$ becomes smaller than f_C^d, static friction is active again.) In the former, static case, the tangential spring is incremented

$$\boldsymbol{\xi}' = \boldsymbol{\xi} + \boldsymbol{v}_t \, \Delta t_{\mathrm{MD}} \;, \tag{1.12}$$

to be used in the next iteration in Eq. (1.8), and the force $\boldsymbol{f}^t = \boldsymbol{f}_{\mathrm{o}}^t$ from Eq. (1.11) is used. In the latter, sliding case, the tangential spring is adjusted to a length which is consistent with Coulombs condition

$$\boldsymbol{\xi}' = -\frac{1}{k_t} f_C^d \, \boldsymbol{t} \;, \tag{1.13}$$

with the tangential unit vector, $\boldsymbol{t} = \boldsymbol{f}_{\mathrm{o}}^t / |\boldsymbol{f}_{\mathrm{o}}^t|$, defined by Eq. (1.11), and thus the magnitude of the Coulomb force is used. Inserting $\boldsymbol{\xi}'$ from Eq. (1.13) into Eq. (1.11) leads to $\boldsymbol{f}_{\mathrm{o}}^t \approx f_C^d \boldsymbol{t} - \gamma_t \boldsymbol{v}_t$. Note that $\boldsymbol{f}_{\mathrm{o}}^t$ and $\boldsymbol{v}_t$ are not necessarily parallel in three dimensions. However, the mapping in Eq. (1.13) works always, rotating the new spring such that the direction of the frictional force is unchanged and, at the same time, limiting the spring in length according to Coulombs law. In short notation the tangential contact law reads

$$\boldsymbol{f}^t = f^t \boldsymbol{t} = +\min\left(f_C, |\boldsymbol{f}_{\mathrm{o}}^t|\right) \boldsymbol{t} \;, \tag{1.14}$$

where f_C follows the static/dynamic selection rules described above.

Note that the tangential force described above is identical to the classical Cundall-Strack spring only in the limits $\mu = \mu^s = \mu^d$ and $\gamma_t = 0$. The sequence of computations and the definitions and mappings into the tangential direction, however, are new to our knowledge in so far that they can be easily used in three dimensions as well as in two.

[2] This is necessary, since the frame of reference of the contact may have rotated since the last time-step

Background Friction

Note that the viscous dissipation takes place in a two-particle contact. In the bulk material, where many particles are in contact with each other, dissipation is very inefficient for long-wavelength cooperative modes of motion [24, 25]. Therefore, an additional damping with the background can be introduced, so that the total force on particle i is

$$\boldsymbol{f}_i = \sum_j \left(f^n \boldsymbol{n} + f^t \boldsymbol{t} \right) - \gamma_b \boldsymbol{v}_i \ , \tag{1.15}$$

with the damping artificially enhanced in the spirit of a rapid relaxation and equilibration. The sum in Eq. (1.15) takes into account all contact partners j of particle i, but the background dissipation can be attributed to the medium between the particles. Note that the effect of γ_b should be checked for each simulation in order to exclude artificial effects. Results of the soft particle method are presented in sections 1.6 and 1.7.

1.3 Hard Sphere Molecular Dynamics

In this section, the hard sphere model is introduced together with the event-driven algorithm. A generalized model takes into account the finite contact duration of realistic particles and, besides providing a physcial parameter, saves computing time because it avoids the "inelastic collapse".

In the framework of the hard sphere model, particles are assumed to be perfectly rigid and they follow an undisturbed motion until a collision occurs as described below. Due to the rigidity of the interaction, the collisions occur instantaneously, so that an event-driven simulation method [26–29] can be used. Note that the ED method was only recently implemented in parallel [28, 30]; however, we avoid to discuss this issue in detail.

The instantaneous nature of hard sphere collisions is artificial, however, it is a valid limit in many circumstances. Even though details of the contact- or collision behavior of two particles are ignored, the hard sphere model is valid when binary collisions dominate and multi-particle contacts are rare [31]. The lack of physical information in the model allows a much simpler treatment of collisions than described in section 1.2 by just using a collision matrix based on momentum conservation and energy loss rules. For the sake of simplicity, we restrict ourselves to smooth hard spheres here. Collision rules for rough spheres are extensively discussed elsewhere, see e.g. [32, 33], and references therein.

1.3.1 Smooth Hard Sphere Collision Model

Between collisions, hard spheres fly independently from each other. A change in velocity – and thus a change in energy – can occur only at a collision. The standard interaction model for instantaneous collisions of identical particles with radius a, and mass m, is used in the following. The post-collisional velocities $\boldsymbol{v}'$ of two collision partners in their center of mass reference frame are given, in terms of the pre-collisional velocities $\boldsymbol{v}$, by

$$\boldsymbol{v}'_{1,2} = \boldsymbol{v}_{1,2} \mp (1+r)\boldsymbol{v}_n \, /2 \ , \tag{1.16}$$

with $\boldsymbol{v}_n \equiv [(\boldsymbol{v}_1 - \boldsymbol{v}_2) \cdot \boldsymbol{n}]\,\boldsymbol{n}$, the normal component of the relative velocity $\boldsymbol{v}_1 - \boldsymbol{v}_2$, parallel to $\boldsymbol{n}$, the unit vector pointing along the line connecting the centers of the colliding particles. If two particles collide, their velocities are changed according to Eq. (1.16), with the change of the translational energy at a collision $\Delta E = -m_{12}(1 - r^2)v_n^2/2$, with dissipation for restitution coefficients $r < 1$.

1.3.2 Event-Driven Algorithm

Since we are interested in the behavior of granular particles, possibly evolving over several decades in time, we use an event-driven (ED) method which discretizes the sequence of events with a variable time step adapted to the problem. This is different from classical MD simulations, where the time step is usually fixed.

In the ED simulations, the particles follow an undisturbed translational motion until an event occurs. An event is either the collision of two particles or the collision of one particle with a boundary of a cell (in the linked-cell structure) [5]. The cells have no effect on the particle motion here; they were solely introduced to accelerate the search for future collision partners in the algorithm.

Simple ED algorithms update the whole system after each event, a method which is straightforward, but inefficient for large numbers of particles. In Ref. [26] an ED algorithm was introduced which updates only those two particles involved in the last collision. Because this algorithm is "asynchronous" in so far that an event, i.e. the *next* event, can occur anywhere in the system, it is so complicated to parallelize it [28]. For the serial algorithm, a double buffering data structure is implemented, which contains the 'old' status and the 'new' status, each consisting of: time of event, positions, velocities, and event partners. When a collision occurs, the 'old' and 'new' status of the participating particles are exchanged. Thus, the former 'new' status becomes the actual 'old' one, while the former 'old' status becomes the 'new' one and is then free for the calculation and storage of possible future events. This seemingly complicated exchange of information is carried out extremely simply and fast by only exchanging the pointers to the 'new' and 'old' status respectively. Note that the 'old' status of particle i has to be kept in memory, in order to update the time of the next contact, t_{ij}, of particle i with any other object j if the latter, independently, changed its status due to a collision with yet another particle. During the simulation such updates may be neccessary several times so that the predicted 'new' status has to be modified.

The minimum of all t_{ij} is stored in the 'new' status of particle i, together with the corresponding partner j. Depending on the implementation, positions and velocities after the collision can also be calculated. This would be a waste of computer time, since before the time t_{ij}, the predicted partners i and j might be involved in several collisions with other particles, so that we apply a delayed update scheme [26]. The minimum times of event, i.e. the times, which indicate the next event for a certain particle, are stored in an ordered heap tree, such that the next event is found at the top of the heap with a computational effort of $O(1)$; changing the position of one particle in the tree from the top to a new position needs $O(\log N)$ operations. The search for possible collision partners is accelerated by the use of a standard linked-cell data structure and consumes $O(1)$ of numerical resources per particle. In total, this results in a numerical effort of $O(N \log N)$ for N particles. For a detailed description of the algorithm see Ref. [26]. Using all these algorithmic tricks, we are able to simulate about

10^5 particles within reasonable time on a low-end PC [34], where the particle number is more limited by memory than by CPU power. Parallelization, however, is a means to overcome the limits of one processor [28].

As a final remark concerning ED, one should note that the disadvantages conncected to the assumptions made that allow to use an event driven algorithm limit the applicability of this method. Within their range of applicability, ED simulations are typically much faster than MD simulations, since the former accounts for a collision in one basic operation (collision matrix), whereas the latter requires about one hundred basic steps (integration time steps). Note that this statement is also true in the dense regime. In the dilute regime, both methods give equivalent results, because collisions are mostly binary [25]. When the system becomes denser, multi-particle collisions can occur and the rigidity assumption within the ED hard sphere approach becomes invalid.

The most striking difference between hard and soft spheres is the fact that soft particles dissipate less energy when they are in contact with many others of their kind. In the following chapter, the so called TC model is discussed as a means to account for the contact duration t_c in the hard sphere model.

1.4 The Link between ED and MD via the TC Model

In the ED method the contact duration is implicitly zero, matching well the corresponding assumption of instantaneous contacts used for the kinetic theory [35, 36]. Due to this artificial simplification (which disregards the fact that a real contact takes always finite time) ED algorithms run into problems when the time between events t_n gets too small: In dense systems with strong dissipation, t_n may even tend towards zero. As a consequence the so-called "inelastic collapse" can occur, i.e. the divergence of the number of events per unit time. The problem of the inelastic collapse [37] can be avoided using restitution coefficients dependent on the time elapsed since the last event [27, 31]. For the contact that occurs at time t_{ij} between particles i and j, one uses $r = 1$ if at least one of the partners involved had a collision with another particle later than $t_{ij} - t_\mathrm{c}$. The time t_c can be seen as a typical duration of a contact, and allows for the definition of the dimensionless ratio

$$\tau_c = t_c/t_n \; . \tag{1.17}$$

The effect of t_c on the simulation results is negligible for large r and small t_c; for a more detailed discussion see [27, 31, 34].

In assemblies of soft particles, multi-particle contacts are possible and the inelastic collapse is avoided. The TC model can be seen as a means to allow for multi-particle collisions in dense systems [27, 38, 39]. In the case of a homogeneous cooling system (HCS), one can explicitly compute the corrected cooling rate (r.h.s.) in the energy balance equation

$$\frac{d}{d\tau}E = -2I(E, t_c) \; , \tag{1.18}$$

with the dimensionless time $\tau = (2/3)At/t_E(0)$ for 3D systems, scaled by $A = (1 - r^2)/4$, and the collision rate $t_E^{-1} = (12/a)\nu g(\nu)\sqrt{T/(\pi m)}$, with $T = 2K/(3N)$. In these units,

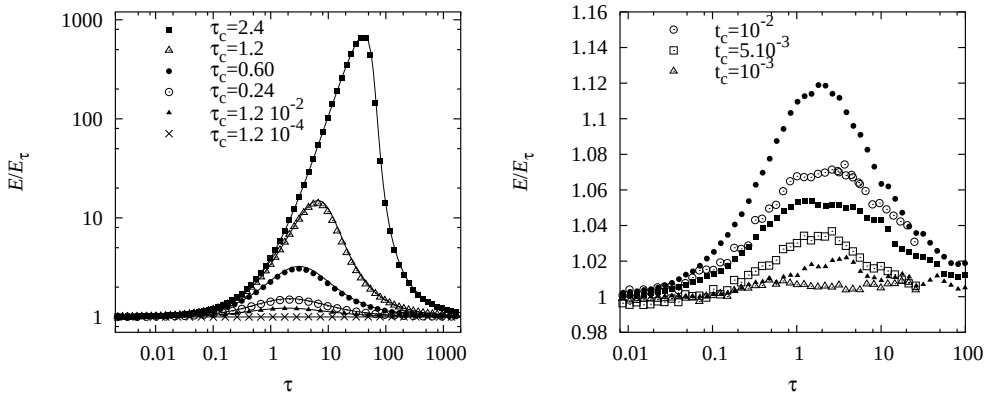

Figure 1.2: (Left) Deviation from the HCS, i.e. rescaled energy E/E_τ, where E_τ is the classical solution $E_\tau = (1+\tau)^{-2}$. The data are plotted against τ for simulations with different $\tau_c(0) = t_c/t_E(0)$ as given in the inset, with $r = 0.99$, and $N = 8000$. Symbols are ED simulation results, the solid line results from the third order correction. (Right) E/E_τ plotted against τ for simulations with $r = 0.99$, and $N = 2197$. Solid symbols are ED simulations, open symbols are MD (soft particle simulations) with three different t_c as given in the inset.

the energy dissipation rate I is a function of the dimensionless energy $E = K/K(0)$ with the kinetic energy K, and the cut-off time t_c. In this representation, the restitution coefficient is hidden in the rescaled time via $A = A(r)$, so that inelastic hard sphere simulations with different r scale on the same master-curve. When the classical dissipation rate $E^{3/2}$ [35] is extracted from I, so that $I(E, t_c) = J(E, t_c)E^{3/2}$, one has the correction-function $J \to 1$ for $t_c \to 0$. The deviation from the classical HCS is [31]:

$$J(E, t_c) = \exp\left(\Psi(x)\right) \ , \tag{1.19}$$

with the series expansion $\Psi(x) = -1.268x + 0.01682x^2 - 0.0005783x^3 + \mathcal{O}(x^4)$ in the collision integral, with $x = \sqrt{\pi} t_c t_E^{-1}(0)\sqrt{E} = \sqrt{\pi}\tau_c(0)\sqrt{E} = \sqrt{\pi}\tau_c$ [31]. This is close to the result $\Psi_{\rm LM} = -2x/\sqrt{\pi}$, proposed by Luding and McNamara, based on probabilistic mean-field arguments [27] [3].

Given the differential equation (1.18) and the correction due to multi-particle contacts from Eq. (1.19), it is possible to obtain the solution numerically, and to compare it to the classical $E_\tau = (1+\tau)^{-2}$ solution. Simulation results are compared to the theory in Fig. 1.2 (left). The agreement between simulations and theory is almost perfect in the examined range of t_c-values, only when deviations from homogeneity are evidenced one expects disagreement between simulation and theory. The fixed cut-off time t_c has no effect when the time between collisions is very large $t_E \gg t_c$, but strongly reduces dissipation when the collisions occur with high frequency $t_E^{-1} \gtrsim t_c^{-1}$. Thus, in the homogeneous cooling state, there is a strong effect initially, and if t_c is large, but the long time behavior tends towards the classical decay $E \to E_\tau \propto \tau^{-2}$.

[3] $\Psi_{\rm LM}$ thus neglects non-linear terms and underestimates the linear part

The final check if the ED results obtained using the TC model are reasonable is to compare them to MD simulations, see Fig. 1.2 (right). Open and solid symbols correspond to soft and hard sphere simulations respectively. The qualitative behavior (the deviation from the classical HCS solution) is identical: The energy decay is delayed due to multi-particle collisions, but later the classical solution is recovered. A quantitative comparison shows that the deviation of E from E_τ is larger for ED than for MD, given that the same t_c is used. This weaker dissipation can be understood from the strict rule used for ED: Dissipation is inactive if any particle had a contact already. The disagreement between ED and MD is systematic and should disappear if an about 30 per-cent smaller t_c value is used for ED. The disagreement is also plausible, since the TC model disregards all dissipation for multi-particle contacts, while the soft particles still dissipate energy - even though much less - in the case of multi-particle contacts.

The above simulations show that the TC model is in fact a "trick" to make hard particles soft and thus connecting between the two types of simulation models: soft and hard. The only change made to traditional ED involves a reduced dissipation for (rapid) multi-particle contacts.

1.5 The Stress in Particle Simulations

The stress tensor is a macroscopic quantity that can be obtained by measurement of forces per area, or via a so-called micro-macro homogenization procedure. Both methods will be discussed below. During derivation, it also turns out that stress has two contributions, the first is the "static stress" due to particle contacts, a *potential energy density*, the second is the "dynamics stress" due to momentum flux, like in the ideal gas, a *kinetic energy density*. For the sake of simplicity, we restrict ourselves to the case of smooth spheres here.

1.5.1 Dynamic Stress

For dynamic systems, one has momentum transport via flux of the particles. This simplest contribution to the stress tensor is the standard stress in an ideal gas, where the atoms (mass points) move with a certain fluctuation velocity $\boldsymbol{v}_i$. The kinetic energy $E = \sum_{i=1}^{N} mv_i^2/2$ due to the fluctuation velocity v_i can be used to define the temperature of the gas $k_B T = 2E/(\mathcal{D}N)$, with the dimension $\mathcal{D}$ and the particle number N. Given a number density $n = N/V$, the stress in the ideal gas is then isotropic and thus quantified by the pressure $p = nk_B T$; note that we will disregard k_B in the following. In the general case, the dynamic stress is $\boldsymbol{\sigma} = (1/V)\sum_i m_i \boldsymbol{v}_i \otimes \boldsymbol{v}_i$, with the dyadic tensor product denoted by '$\otimes$', and the pressure $p = \mathrm{tr}\boldsymbol{\sigma}/\mathcal{D} = nT$ is the kinetic energy density.

The additional contribution to the stress is due to collisions and contacts and will be derived from the principle of virtual displacement for soft interaction potentials below, and then be modified for hard sphere systems.

1.5.2 Static Stress from Virtual Displacements

From the centers of mass $\boldsymbol{r}_1$ and $\boldsymbol{r}_2$ of two particles, we define the so-called branch vector $\boldsymbol{l} = \boldsymbol{r}_1 - \boldsymbol{r}_2$, with the reference distance $l = |\boldsymbol{l}| = 2a$ at contact, and the corresponding unit vector $\boldsymbol{n} = \boldsymbol{l}/l$. The deformation in the normal direction, relative to the reference configuration, is defined as $\boldsymbol{\delta} = 2a\boldsymbol{n} - \boldsymbol{l}$. A virtual change of the deformation is then

$$\partial\boldsymbol{\delta} = \boldsymbol{\delta}' - \boldsymbol{\delta} \approx \partial\boldsymbol{l} = \boldsymbol{\varepsilon} \cdot \boldsymbol{l} \,, \tag{1.20}$$

where the prime denotes the deformation after the virtual displacement described by the tensor $\boldsymbol{\varepsilon}$. The corresponding potential energy density due to the contacts of one pair of particles is $u = k\boldsymbol{\delta}^2/(2V)$, expanded to second order in $\boldsymbol{\delta}$, leading to the virtual change

$$\partial u = \frac{k}{V}\left(\boldsymbol{\delta} \cdot \partial\boldsymbol{\delta} + \frac{1}{2}(\partial\delta)^2\right) \approx \frac{k}{V}\,\boldsymbol{\delta} \cdot \partial\boldsymbol{l}^n \,, \tag{1.21}$$

where k is the spring stiffness (the prefactor of the quadratic term in the series expansion of the interaction potential), V is the averaging volume, and $\partial\boldsymbol{l}^n = \boldsymbol{n}(\boldsymbol{n} \cdot \boldsymbol{\varepsilon} \cdot \boldsymbol{l})$ is the normal component of $\partial\boldsymbol{l}$. Note that ∂u depends only on the normal component of $\partial\boldsymbol{\delta}$ due to the scalar product with $\boldsymbol{\delta}$, which is parallel to $\boldsymbol{n}$.

From the potential energy density, we obtain the stress from a virtual deformation by differentiation with respect to the deformation tensor components

$$\boldsymbol{\sigma} = \frac{\partial u}{\partial\boldsymbol{\varepsilon}} = \frac{k}{V}\boldsymbol{\delta} \otimes \boldsymbol{l} = \frac{1}{V}\boldsymbol{f} \otimes \boldsymbol{l} \,, \tag{1.22}$$

where $\boldsymbol{f} = k\boldsymbol{\delta}$ is the force acting at the contact, and the dyadic product $\otimes$ of two vectors leads to a tensor of rank two.

1.5.3 Stress for Soft and Hard Spheres

Combining the dynamic and the static contributions to the stress tensor [40], one has for smooth, soft spheres:

$$\boldsymbol{\sigma} = \frac{1}{V}\left[\sum_i m_i \boldsymbol{v}_i \otimes \boldsymbol{v}_i - \sum_{c \in V} \boldsymbol{f}_c \otimes \boldsymbol{l}_c\right] \,, \tag{1.23}$$

where the right sum runs over all contacts c in the averaging volume V. Replacing the force vector by momentum change per unit time, one obtains for hard spheres:

$$\boldsymbol{\sigma} = \frac{1}{V}\left[\sum_i m_i \boldsymbol{v}_i \otimes \boldsymbol{v}_i - \frac{1}{\Delta t}\sum_n \sum_j \boldsymbol{p}_j \otimes \boldsymbol{l}_j\right] \,, \tag{1.24}$$

where $\boldsymbol{p}_j$ and $\boldsymbol{l}_j$ are the momentum change and the center-contact vector of particle j at collision n, respectively. The sum in the left term runs over all particles i, the first sum in the right term runs over all collisions n occurring in the averaging time Δt, and the second sum in the right term concerns the collision partners of collision n [27].
Exemplary stress computations from MD and ED simulations are presented in the following section.

1.6 2D Simulation Results

Stress computations from two dimensional MD and ED simulations are presented in the following subsections. First, a global equation of state, valid for all densities, is proposed based on ED simulations, and second, the stress tensor from a slow, quasi-static deformation is computed from MD simulations with frictional particles.

1.6.1 The Equation of State from ED

The mean pressure in two dimensions is $p = (\sigma_1 + \sigma_2)/2$, with the eigenvalues σ_1 and σ_2 of the stress tensor [4, 40, 41]. The 2D dimensionless, reduced pressure $P = p/(nT) - 1 = pV/E - 1$ contains only the collisional contribution and the simulations agree nicely with the theoretical prediction $P_2 = 2\nu g_2(\nu)$ for elastic systems, with the pair-correlation function $g_2(\nu) = (1 - 7\nu/16)/(1 - \nu)^2$, and the volume fraction $\nu = N\pi a^2/V$, see Fig. 1.3. A better pair-correlation function is

$$g_4(\nu) = \frac{1 - 7\nu/16}{(1-\nu)^2} - \frac{\nu^3/16}{8(1-\nu)^4} \ , \tag{1.25}$$

which defines the non-dimensional collisional stress $P_4 = 2\nu g_4(\nu)$. For a system with homogeneous temperature, as a remark, the collision rate is proportional to the dimensionless pressure $t_n^{-1} \propto P$.

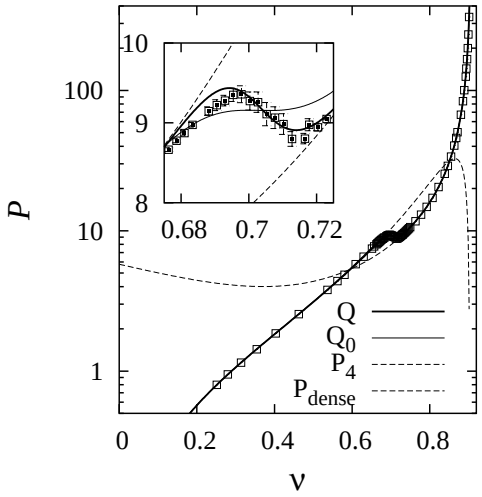

Figure 1.3: The dashed lines are P_4 and $P_{\rm dense}$ as functions of the volume fraction ν, and the symbols are simulation data, with standard deviations as given by the error bars in the inset. The thick solid line is Q, the corrected global equation of state from Eq. (1.26), and the thin solid line is Q_0 without empirical corrections.

When plotting P against ν with a logarithmic vertical axis, in Fig. 1.3, the simulation results can almost not be distinguished from P_2 for $\nu < 0.65$, but P_4 leads to better agreement

up to $\nu = 0.67$. Crystallization is evidenced at the point of the liquid-solid transition $\nu_c \approx 0.7$, and the data clearly deviate from P_4. The pressure is strongly reduced due to the increase of free volume caused by ordering. Eventually, the data diverge at the maximum packing fraction $\nu_{\max} = \pi/(2\sqrt{3})$ for a perfect triangular array.

For high densities, one can compute from free-volume models, the reduced pressure $P_{\rm fv} = 2\nu_{\max}/(\nu_{\max} - \nu)$. Slightly different functional forms do not lead to much better agreement [41]. Based on the numerical data, we propose the corrected high density pressure $P_{\rm dense} = P_{\rm fv} h(\nu_{\max} - \nu) - 1$, with the empirical fit function $h(x) = 1 + c_1 x + c_3 x^3$, and $c_1 = -0.04$ and $c_3 = 3.25$, in perfect agreement with the simulation results for $\nu \geq 0.73$.

Since, to our knowledge, there is no conclusive theory available to combine the disordered and the ordered regime [42], we propose a global equation of state

$$Q = P_4 + m(\nu)[P_{\rm dense} - P_4] \,, \tag{1.26}$$

with an empirical merging function $m(\nu) = [1 + \exp(-(\nu - \nu_c)/m_0)]^{-1}$, which selects P_4 for $\nu \ll \nu_c$ and $P_{\rm dense}$ for $\nu \gg \nu_c$, with the transition density ν_c and the width of the transition m_0. In Fig. 1.3, the fit parameters $\nu_c = 0.702$ and $m_0 \approx 0.062$ lead to qualitative and quantitative agreement between Q (thick line) and the simulation results (symbols). However, a simpler version $Q_0 = P_2 + m(\nu)[P_{\rm fv} - P_2]$, (thin line) without empirical corrections leads already to reasonable agreement when $\nu_c = 0.698$ and $m_0 = 0.0125$ are used. In the transition region, this function Q_0 has no negative slope but is continuous and differentiable, so that it allows for an easy and compact numerical integration of P. We selected the parameters for Q_0 as a compromise between the quality of the fit on the one hand and the simplicity and treatability of the function on the other hand.

As an application of the global equation of state, the density profile of a dense granular gas in the gravitational field has been computed for monodisperse [40] and bidisperse situations [4, 41]. In the latter case, however, segregation was observed and the mixture theory could not be applied. The equation of state and also other transport properties are extensively discussed in Refs. [43–46] for 2D, bi-disperse systems.

1.6.2 Quasi-static MD simulations

In contrast to the dynamic, collisional situation discussed in the previous section, a quasi-static situation, with all particles almost at rest most of the time, is discussed in the following.

Model Parameters

The systems examined in the following contain $N = 1950$ particles with radii a_i randomly drawn from a homogeneous distribution with minimum $a_{\min} = 0.5\,10^{-3}\,\mathrm{m}$ and maximum $a_{\max} = 1.5\,10^{-3}\,\mathrm{m}$. The masses $m_i = (4/3)\rho\pi a_i^3$, with the density $\rho = 2.0\,10^3\,\mathrm{kg\,m^{-3}}$, are computed as if the particles were spheres. This is an artificial choice and introduces some dispersity in mass in addition to the dispersity in size. Since we are mainly concerned about slow deformation and equilibrium situations, the choice for the calculation of mass should not matter. The total mass of the particles in the system is thus $M \approx 0.02\,\mathrm{kg}$ with the typical reduced mass of a pair of particles with mean radius, $m_{12} \approx 0.42\,10^{-5}\,\mathrm{kg}$. If not explicitly

mentioned, the material parameters are $k_2 = 10^5\,\mathrm{N\,m^{-1}}$ and $\gamma_0 = 0.1\,\mathrm{kg\,s^{-1}}$. The other spring-constants k_1 and k_c will be defined in units of k_2. In order to switch on cohesion, $k_1 < k_2$ and $k_c > 0$ is used; if not mentioned explicitly, $k_1 = k_2/2$ is used, and k_2 is constant, independent of the maximum overlap previously achieved.

Using the parameters $k_1 = k_2$ and $k_c = 0$ in Eq. (1.4) leads to a typical contact duration (half-period): $t_c \approx 2.03\,10^{-5}\,\mathrm{s}$ for $\gamma_0 = 0$, $t_c \approx 2.04\,10^{-5}\,\mathrm{s}$ for $\gamma_0 = 0.1\,\mathrm{kg\,s^{-1}}$, and $t_c \approx 2.21\,10^{-5}\,\mathrm{s}$ for $\gamma_0 = 0.5\,\mathrm{kg\,s^{-1}}$ for a collision. Accordingly, an integration time-step of $t_{\mathrm{MD}} = 5\,10^{-7}\,\mathrm{s}$ is used, in order to allow for a 'safe' integration of contacts involving smaller particles. Large values of k_c lead to strong cohesive forces, so that also more energy can be dissipated in one collision. The typical response time of the particle pairs, however, is not affected so that the numerical integration works well from a stability and accuracy point of view.

Boundary Conditions

The experiment chosen is the bi-axial box set-up, see Fig. 1.4, where the left and bottom walls are fixed, and stress- or strain-controlled deformation is applied. In the first case a wall is subject to a predefined pressure, in the second case, the wall is subject to a pre-defined strain. In a typical 'experiment', the top wall is strain controlled and slowly shifted downwards while the right wall moves stress controlled, dependent on the forces exerted on it by the material in the box. The strain-controlled position of the top wall as function of time t is here

$$z(t) = z_{\mathrm{f}} + \frac{z_0 - z_{\mathrm{f}}}{2}(1 + \cos\omega t)\,, \quad \text{with} \quad \varepsilon_{zz} = 1 - \frac{z}{z_0}\,, \tag{1.27}$$

where the initial and the final positions z_0 and z_{f} can be specified together with the rate of deformation $\omega = 2\pi f$ so that after a half-period $T/2 = 1/(2f)$ the extremal deformation is reached. With other words, the cosine is active for $0 \le \omega t \le \pi$. For larger times, the top-wall is fixed and the system can relax indefinitely. The cosine function is chosen in order to allow for a smooth start-up and finish of the motion so that shocks and inertia effects are reduced, however, the shape of the function is arbitrary as long as it is smooth.

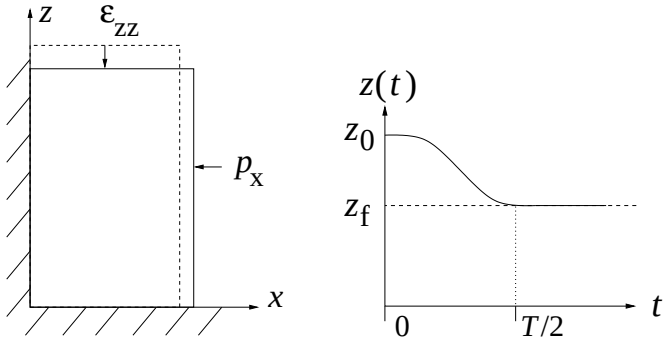

Figure 1.4: (Left) Schematic drawing of the model system. (Right) Position of the top-wall as function of time for the strain-controlled situation.

The stress-controlled motion of the side-wall is described by

$$m_{\mathrm{w}}\ddot{x}(t) = F_{\mathrm{x}}(t) - p_{\mathrm{x}}z(t) - \gamma_{\mathrm{w}}\dot{x}(t) \ , \tag{1.28}$$

where m_{w} is the mass of the right side wall. Large values of m_{w} lead to slow adaption, small values allow for a rapid adaption to the actual situation. Three forces are active: (i) the force $F_{\mathrm{x}}(t)$ due to the bulk material, (ii) the force $-p_{\mathrm{x}}z(t)$ due to the external pressure, and (iii) a strong frictional force which damps the motion of the wall so that oscillations are reduced.

Initial Configuration

Initially, the particles are randomly distributed in a huge box, with rather low overall density. Then the box is compressed, either by moving the walls to their desired position, or by defining an external pressure $p = p_{\mathrm{x}} = p_{\mathrm{z}}$, in order to achieve an isotropic initial condition. Starting from a relaxed, isotropic initial configuration, the strain is applied to the top wall and the response of the system is examined. In Fig. 1.5, snapshots from a typical simulation are shown during compression.

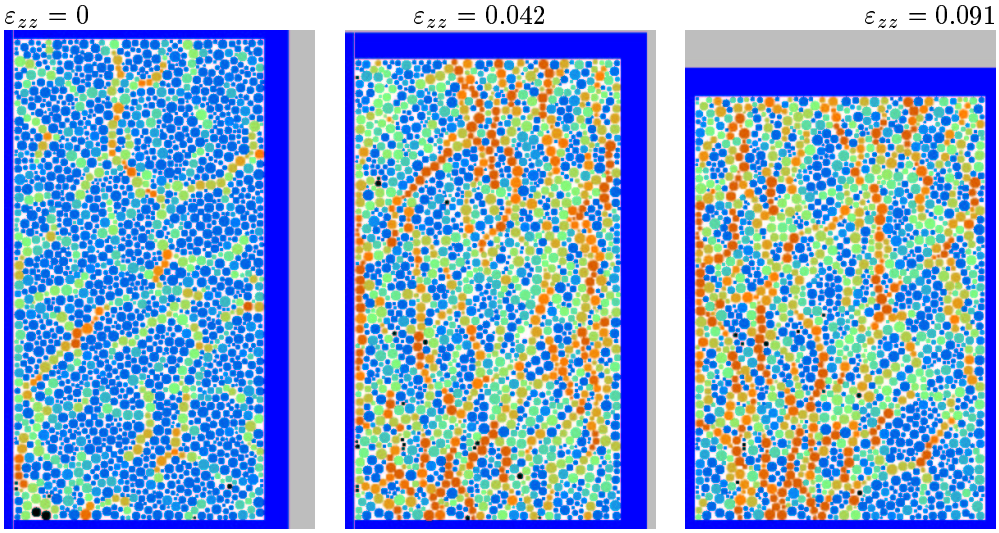

Figure 1.5: Snapshots of the simulation at different ε_{zz} for constant side pressure p. The color code corresponds to the potential energy of each particle, decaying from red over green to blue and black. The latter black particles are so-called rattlers that do not contribute to the static contact network.

In the following, simulations are presented with different side pressures $p = 20$, 40, 100, 200, 400, and 500. The behavior of the averaged scalar and tensor variables during the simulations is examined in more detail for situations with small and large confining pressure. The averages are performed such that ten to twenty per-cent of the total volume are disregarded in the vicinity of each wall in order to avoid boundary effects. A particle contact is taken into account for the average if the contact point lies within the averaging volume V.

Compression and Dilation

The first quantity of interest is the density (volume fraction) ν and, related to it, the volumetric strain $\varepsilon_V = \Delta V/V$. From the averaged data, we evidence compression for small deformation and large side pressure. This initial regime follows strong dilation, for all pressures, until a quasi-steady-state is reached, where the density is almost constant besides a weak tendency towards further dilation.

An initially dilute granular medium (weak confining pressure) thus shows dilation from the beginning, whereas a denser granular material (strong confining pressure) can be compressed even further by the relatively strong external forces until dilation starts. The range of density changes is about 0.02 in volume fraction and spans up to 3 % changes in volumetric strain.

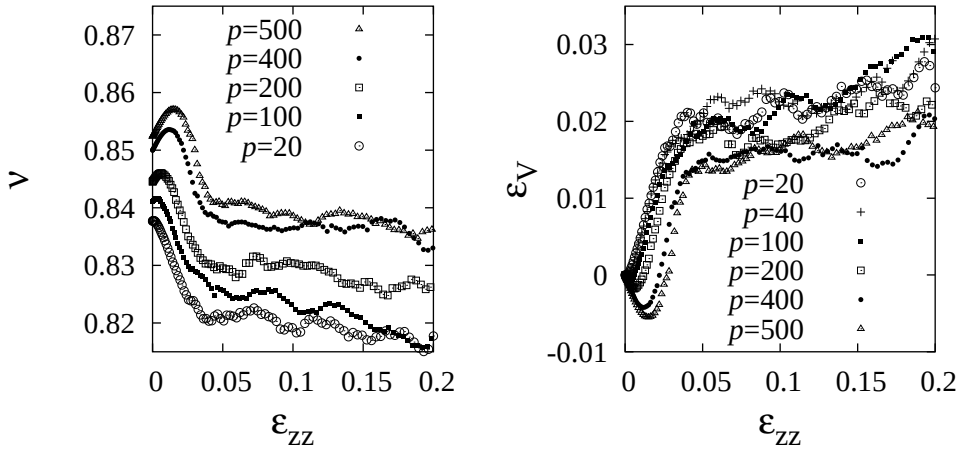

Figure 1.6: (Left) Volume fraction $\nu = \sum_i \pi a_i^2/V$ for different confining pressure p. (Right) Volumetric strain – negative values mean compression, whereas positive values correspond to dilation.

From the initial slope, one can obtain the Poisson ratio of the bulk material, and from the slope in the dilatant regime, one obtains the so-called dilatancy angle, a measure of the magnitude of dilatancy required before shear is possible [47, 48].

Stress Tensor

The sums of the normal and the tangential stress-contributions are displayed in Fig. 1.7 for two side-pressures $p = 20$ and $p = 200$. The lines show the stress measured on the walls, and the symbols correspond to the stress measured via the micro-macro average in Eq. (1.23), proving the reasonable quality of the micro-macro transition as compared to the wall stress "measurement".

There is also other macroscopic information hidden in the stress-strain curves in Fig. 1.7. From the initial, rapid increase in stress, one can determine the compressibility of the bulk-material. Later, the stress reaches a peak at approximately $2.6p$ and then saturates at about

$2p$. From both peak- and saturation stress, one obtains the yield stresses at peak and in critical state flow, respectively [49].

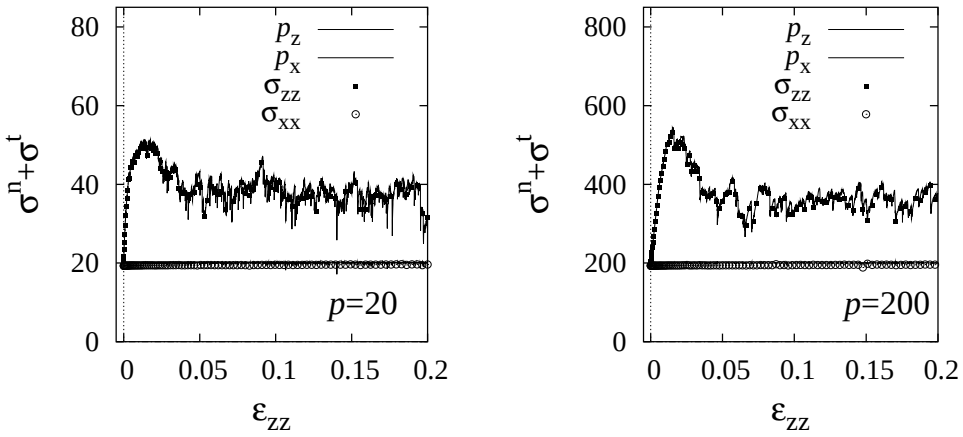

Figure 1.7: Total stress tensor $\boldsymbol{\sigma} = \boldsymbol{\sigma}^n + \boldsymbol{\sigma}^t$ for small (Left) and high (Right) pressure – the agreement between the wall pressure and the averaged stress is almost perfect.

Note that for the parameters used here, both the dynamic stress and the tangential contributions to the stress tensor are more than one order of magnitude smaller than the normal contributions. As a cautionary note, we remark also that the artificial stress induced by the background viscous force is negligible here (about two per-cent), when $\gamma_b = 10^{-3}\,\mathrm{kg\,s^{-1}}$ and a compression frequency $f = 0.1\,\mathrm{s^{-1}}$ are used. For faster compression with $f = 0.5\,\mathrm{s^{-1}}$, one obtains about ten per-cent contribution to stress from the artificial background force.

1.7 Large-Scale Computational Examples

In this section, several examples of rather large particle numbers simulated with MD and ED are presented. The ED algorithm is first used to simulate a freely cooling dissipative gas in two and three dimensions [29, 34]. Then, a peculiar three dimensional ring-shear experiment is modeled with soft sphere MD.

1.7.1 Cluster Growth (ED)

In the following, a two-dimensional system of length $L = l/d = 560$ with $N = 99856$ dissipative particles of diameter $d = 2a$ is examined [27, 34], with volume fraction $\nu = 0.25$ and restitution coefficient $r = 0.9$. This 2D system is compared to a three-dimensional system of length $L = l/d = 129$ with $N = 512000$ dissipative spheres of diameter d and volume fraction $\nu = 0.25$ with $r = 0.3$ [29].

Initial configuration

Initially the particles are arranged on a square lattice with random velocities drawn from an interval with constant probability for each coordinate. The mean total velocity, i.e. the random momentum due to the fluctuations, is eliminated in order to have a system with its center of mass at rest. The system is allowed to evolve for some time, until the arbitrary initial condition is forgotten, i.e. the density is homogeneous, and the velocity distribution is a Gaussian in each coordinate. Then dissipation is switched on and the evolution of the system is reported for the selected r. In order to avoid the inelastic collapse, the TC model is used, which reduces dissipation if the time between collisions drops below a value of $t_c = 10^{-5}$ s.

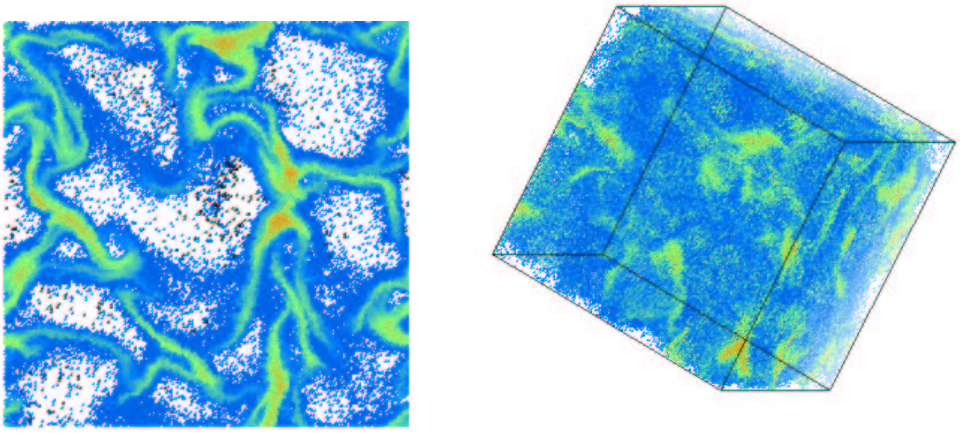

Figure 1.8: (Left) Collision frequency of individual particles from a 2D simulation, after about 5200 collisions per particle. (Right) Cluster visualization from a 3D simulation. The colors in both panels indicate large (red), medium (green), and small (blue) collision rates.

System evolution

For the values of r used here, the system becomes inhomogeneous quite rapidly [29, 34]. Clusters, and thus also dilute regions, build up and have the tendency to grow. Since the system is finite, their extension will reach system size at a finite time. Thus we distinguish between three regimes of system evolution: (i) the initially (almost) homogeneous state, (ii) the cluster growth regime, and (iii) the system size dependent final stage where the clusters have reached system size. We note that a cluster does not behave like a solid body, but has internal motion and can eventually break into pieces after some time. These pieces (small clusters) collide and can merge to larger ones.

In Fig. 1.8, snapshots are presented and the collision rate is color-coded. The collision rate and the pressure are higher inside the clusters than at their surface. Note that most of the computational effort is spent in predicting collisions and to compute the velocities after

the collisions. Therefore, the regions with the largest collision frequencies require the major part of the computational resources. Due to the TC model, this effort stays limited and the simulations can easily continue for many thousand collisions per particle.

1.7.2 3D ring shear cell simulation

The simulation in this section models a ring-shear cell experiment, as recently proposed [50, 51]. The interesting observation in the experiment is a universal shear zone, initiated at the bottom of the cell and becoming wider and moving inwards while propagating upwards in the system.

Model system

The numerical model chosen here is MD with smooth particles in three dimensions. In order to save computing time, only a quarter of the ring-shaped geometry is simulated. The walls are cylindrical, and are rough on the particle scale due to some attached particles. The outer cylinder wall with radius R_o, and part of the bottom $r > R_s$ are rotating around the symmetry axis, while the inner wall with radius R_i, and the attached bottom-disk $r < R_s$ remain at rest. In order to resemble the experiment, the geometry data are $R_i = 0.0147\,\mathrm{m}$, $R_s = 0.085\,\mathrm{m}$, and $R_o = 0.110\,\mathrm{m}$. Note that the small R_i value is artificial, but it does not affect the results for small and intermediate filling heights.

The slit in the bottom wall at $r = R_s$ triggers a shear band. In order to examine the behavior of the shear band as function of the filling height H, this system is filled with 6000 to 64000 spherical particles with mean radius 1.0 mm and radii range $0.5\,\mathrm{mm} < a < 1.5\,\mathrm{mm}$, which interact here via repulsive and dissipative forces only. The particles are forced towards the bottom by the gravity force $\boldsymbol{f}_g = m\boldsymbol{g}$ here and are kept inside the system by the cylindrical walls. In order to provide some wall roughness, a fraction of the particles (about 3 per-cent) that are originally in contact with the walls are glued to the walls and move with them.

Material and system parameters

The material parameters for the particle-particle and -wall interactions are $k = 10^2\,\mathrm{N/m}$ and $\gamma_0 = 2.10^{-3}\,\mathrm{kg/s}$. Assuming a collision of the largest and the smallest particle used, the reduced mass $m_{12} = 2.94\,10^{-6}\,\mathrm{kg}$, leads to a typical contact duration $t_c = 5.4\,10^{-4}\,\mathrm{s}$ and a restitution coefficient of $r = 0.83$. The integration time step is $t_{\mathrm{MD}} = 5.10^{-6}\,\mathrm{s}$, i.e. two orders of magnitude smaller than the contact duration.

The simulations run for 25 s with a rotation rate $f_o = 0.01\,\mathrm{s}^{-1}$ of the outer cylinder, with angular velocity $\Omega_o = 2\pi f_o$. For the average of the displacement, only times $t > 10\,\mathrm{s}$ are taken into account. Within the averaging accuracy, the system seemingly has reached a quasi-steady state after about 8 s. The empty cell is shown in Fig. 1.9, while three realizations with different filling height are displayed in Fig. 1.10, both as top- and front-view.

Shear deformation results

From the top-view, it is evident that the shear band moves inwards with increasing filling height, and it also becomes wider. From the front-view, the same information can be evi-

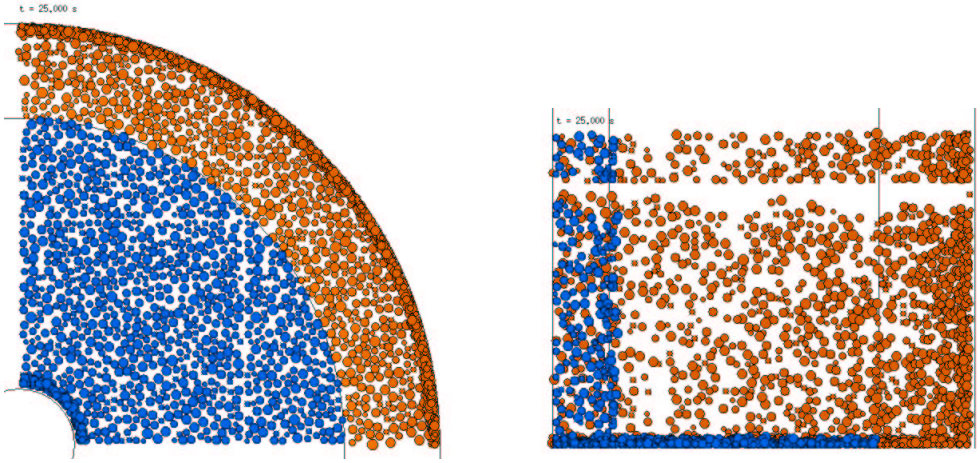

Figure 1.9: Snapshots from the quarter-cylinder geometry. Visible are here only those particles glued to the wall; the cylinder and slit positions are indicated by the lines. (Left) Top-view and (Right) front-view. The colors blue and red correspond to static and moving wall particles.

denced and, in addition, the shape of the shear band inside the bulk is visible: The inwards displacement happens deep in the bulk and the position of the shear band is not changing a lot closer to the surface.

In order to allow for a more quantitative analysis of the shear band, both on the top and as function of depth, we perform fits with the universal shape function proposed in [50]:

$$\frac{v_\varphi(r)}{r\Omega_o} = A\left(1 + \mathrm{erf}\left(\frac{r - R_c}{W}\right)\right) , \tag{1.29}$$

where A is a dimensionless amplitude $A = 0.50 \pm 0.02$, R_c is the center of the shearband, and W its width.

The fits to the simulations confirm qualitatively the experimental findings in so far that the center of the shear band, as observed on top of the material, see Fig. 1.11, moves inwards with a $R_c \propto H^{5/2}$ behavior, and that the width of the shear band increases almost linearly with H. For filling heights larger than $H \approx 0.05\,\mathrm{m}$, deviations from this behavior are observed, because the inner cylinder is reached and thus sensed by the shearband. Slower shearing does not affect the center, but reduces slightly the width - as checked by one simulation.

Like in the experiments, the behavior of the shearband within the bulk, see Fig. 1.12, deviates qualitatively from the behavior seen from the top. Instead of a slow motion of the shear band center inwards, the shear band rapidly moves inwards at small heights h, and reaches a saturation distance with small change closer to the surface. Again, a slower rotation does not affect the center but reduces the width.

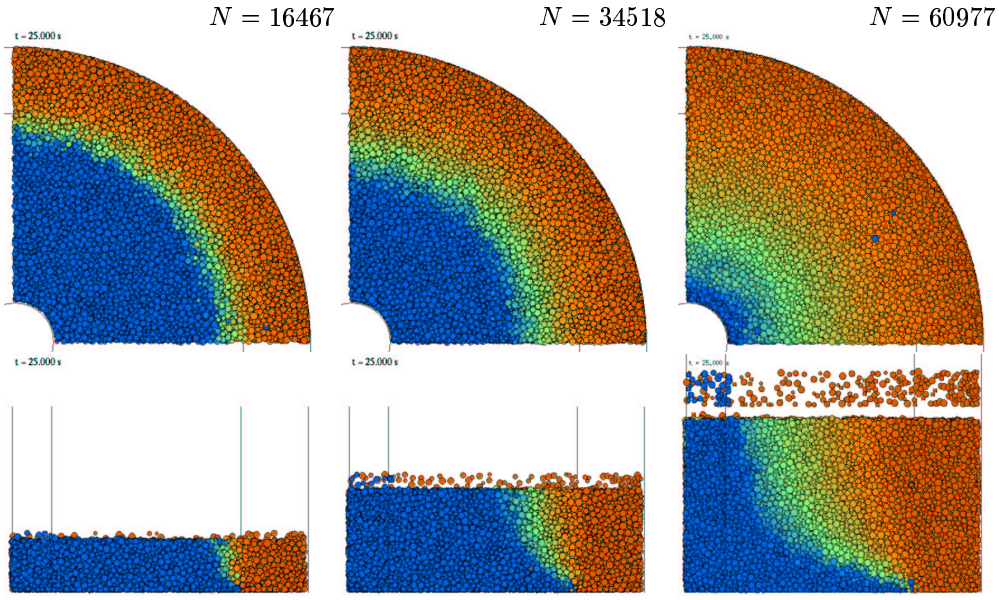

Figure 1.10: Snapshots from simulations with different filling heights seen from the top and from the front, and the particle number N is given in the inset. The colors blue, green, orange and red denote particles with $r\mathrm{d}\phi \leq 0.5\,\mathrm{mm}$, $r\mathrm{d}\phi \leq 2\,\mathrm{mm}$, $r\mathrm{d}\phi \leq 4\,\mathrm{mm}$, and $r\mathrm{d}\phi > 4\,\mathrm{mm}$, i.e. the displacement in tangential direction per second, respectively. The filling heights in these simulations are $H = 0.018\,\mathrm{m}$, $0.037\,\mathrm{m}$, and $0.061\,\mathrm{m}$ (from left to right).

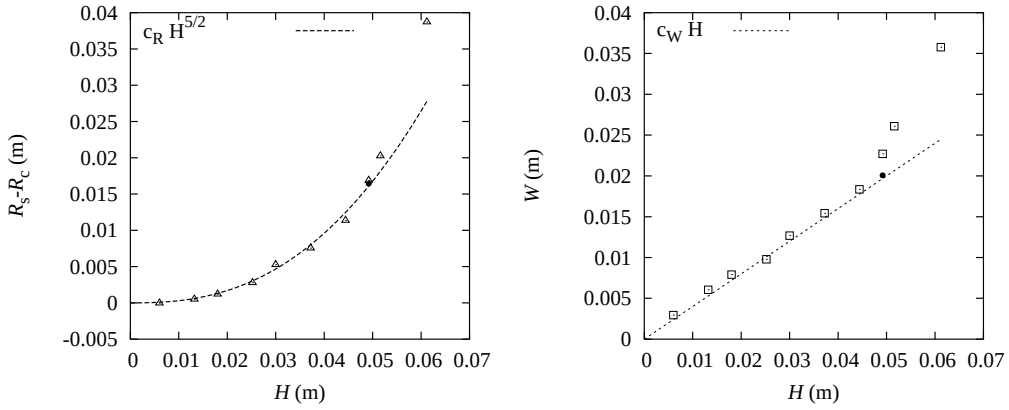

Figure 1.11: (Left) Distance of the top-layer shearband center from the slit, both plotted against the filling height H. The open symbols are simulation results, the solid symbol is a simulation with slower rotation $f_o = 0.005\,\mathrm{s}^{-1}$, and the line is a fit with constant $c_R = 30$. (Right) Width of the shearband from the same simulations; the line is a fit with $c_W = 2/5$.

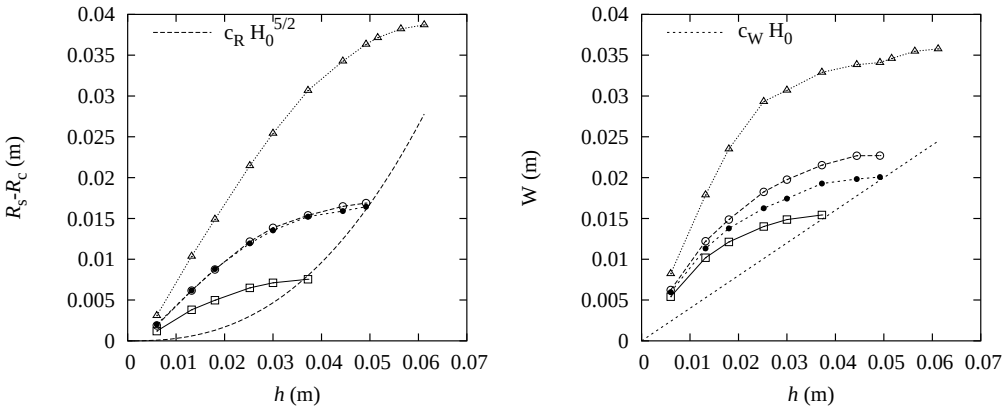

Figure 1.12: (Left) Distance of the bulk shearband center from the slit and, (Right) width of the shearband, both plotted against the height h. The open symbols are simulation results obtained with $f_o = 0.01\,\mathrm{s}^{-1}$, the solid symbols are obtained with slower rotation $f_o = 0.005\,\mathrm{s}^{-1}$. Squares, circles and triangles correspond to the filling heights $H = 0.037\,\mathrm{m}$, $0.049\,\mathrm{m}$, and $0.061\,\mathrm{m}$, respectively. The curves are identical to those plotted in Fig. 1.11.

Discussion

In summary, the example of a ring shear cell simulation in 3D has shown, that even without the more complicated details of fancy interaction laws, experiments can be reproduced at least qualitatively. A more detailed study of quantitative agreement has been performed in 2D [15], and is in progress for the 3D case. A challenge for the future remains the micro-macro transition in 3D and the continuum theory formulation of the shear band problem.

1.8 Conclusion

The chapter *Molecular Dynamics Simulations of Granular Materials* is a summary of the most important details about soft particle molecular dynamics (MD) and hard particle event driven (ED) simulations, together with an attempt to link the two approaches in the dense limit where multi-particle contacts become important.

As an example for a micro-macro transition, the stress tensor was defined and computed for dynamic and quasi-static systems, using ED and MD, respectively. This led, for example, to a global equation of state, valid for all attainable densities, and also to the partial stresses due to normal and tangential (frictional) contacts. For the latter situation, the micro-macro average is compared to the macroscopic stress (=force/area) measurement, with reasonable agreement. In the last section, some examples of larger simulations are provided in order to illustrate applications at the front of ongoing research, as there are: cluster formation, or shear band formation.

In conclusion, molecular dynamics methods have proven a helpful tool for the understanding of granular systems. The qualitative approach of the early years has now developed into the attempt of a quantitative predictive modeling of the diverse modes of complex behavior in

granular media. To achieve this goal will be a research challenge for the next decades, involving enhanced kinetic theories for dense collisional flows and elaborate constitutive models for quasi-static, dense systems with shear band localisation.

Acknowledgements

We acknowledge the financial support of several funding institutions that supported the reviewed research, and also the helpful discussions with the many persons that contributed to these results.

Bibliography

[1] P. A. Vermeer, S. Diebels, W. Ehlers, H. J. Herrmann, S. Luding, and E. Ramm, editors. *Continuous and Discontinuous Modelling of Cohesive Frictional Materials*, Berlin, 2001. Springer. Lecture Notes in Physics 568.

[2] T. Pöschel and S. Luding, editors. *Granular Gases*, Berlin, 2001. Springer. Lecture Notes in Physics 564.

[3] J. G. Kirkwood, F. P. Buff, and M. S. Green. The statistical mechanical theory of transport processes. *J. Chem. Phys.*, 17(10):988, 1949.

[4] S. Luding, M. Lätzel, and H. J. Herrmann. From discrete element simulations towards a continuum description of particulate solids. In A. Levy and H. Kalman, editors, *Handbook of Conveying and Handling of Particulate Solids*, pages 39–44, Amsterdam, The Netherlands, 2001. Elsevier.

[5] M. P. Allen and D. J. Tildesley. *Computer Simulation of Liquids*. Oxford University Press, Oxford, 1987.

[6] D. C. Rapaport. *The Art of Molecular Dynamics Simulation*. Cambridge University Press, Cambridge, 1995.

[7] M. Lätzel, S. Luding, and H. J. Herrmann. Macroscopic material properties from quasi-static, microscopic simulations of a two-dimensional shear-cell. *Granular Matter*, 2(3):123–135, 2000. cond-mat/0003180.

[8] P. A. Cundall and O. D. L. Strack. A discrete numerical model for granular assemblies. *Géotechnique*, 29(1):47–65, 1979.

[9] Y. M. Bashir and J. D. Goddard. A novel simulation method for the quasi-static mechanics of granular assemblages. *J. Rheol.*, 35(5):849–885, 1991.

[10] S. van Baars. *Discrete Element Analysis of Granular Materials*. PhD thesis, Technische Universiteit Delft, Delft, Nederlands, 1996.

[11] H. J. Herrmann and S. Luding. Modeling granular media with the computer. *Continuum Mechanics and Thermodynamics*, 10:189–231, 1998.

[12] C. Thornton. Numerical simulations of deviatoric shear deformation of granular media. *Géotechnique*, 50(1):43–53, 2000.

[13] C. Thornton and S. J. Antony. Quasi-static deformation of a soft particle system. *Powder Technology*, 109(1-3):179–191, 2000.

[14] C. Thornton and L. Zhang. A dem comparison of different shear testing devices. In Y. Kishino, editor, *Powders & Grains 2001*, pages 183–190, Rotterdam, 2001. Balkema.

[15] M. Lätzel, S. Luding, H. J. Herrmann, D. W. Howell, and R. P. Behringer. Comparing simulation and experiment of a 2d granular couette shear device. *Eur. Phys. J. E*, 11(4):325–333, 2003.

[16] S. Luding. Collisions & contacts between two particles. In H. J. Herrmann, J.-P. Hovi, and S. Luding, editors, *Physics of dry granular media - NATO ASI Series E350*, page 285, Dordrecht, 1998. Kluwer Academic Publishers.

[17] O. R. Walton and R. L. Braun. Viscosity, granular-temperature, and stress calculations for shearing assemblies of inelastic, frictional disks. *Journal of Rheology*, 30(5):949–980, 1986.

[18] Jürgen Tomas. Particle adhesion fundamentals and bulk powder consolidation. *KONA*, 18:157–169, 2000.

[19] C. Y. Zhu, A. Shukla, and M. H. Sadd. Prediction of dynamic contact loads in granular assemblies. *J. of Applied Mechanics*, 58:341, 1991.

[20] M. H. Sadd, Q. M. Tai, and A. Shukla. Contact law effects on wave propagation in particulate materials using distinct element modeling. *Int. J. Non-Linear Mechanics*, 28(2):251, 1993.

[21] S. Luding, K. Manetsberger, and J. Müllers. A disrete model for long time sintering. submitted, 2004.

[22] L. Brendel and S. Dippel. Lasting contacts in molecular dynamics simulations. In H. J. Herrmann, J.-P. Hovi, and S. Luding, editors, *Physics of Dry Granular Media*, page 313, Dordrecht, 1998. Kluwer Academic Publishers.

[23] N. V. Brilliantov and T. Pöschel. Rolling friction of a viscous sphere on a hard plane. *Europhys. Lett.*, 42:511–516, 1998.

[24] S. Luding, E. Clément, A. Blumen, J. Rajchenbach, and J. Duran. The onset of convection in molecular dynamics simulations of grains. *Phys. Rev. E*, 50:R1762, 1994.

[25] S. Luding, E. Clément, A. Blumen, J. Rajchenbach, and J. Duran. Anomalous energy dissipation in molecular dynamics simulations of grains: The "detachment effect". *Phys. Rev. E*, 50:4113, 1994.

[26] B. D. Lubachevsky. How to simulate billards and similar systems. *J. of Comp. Phys.*, 94(2):255, 1991.

[27] S. Luding and S. McNamara. How to handle the inelastic collapse of a dissipative hard-sphere gas with the TC model. *Granular Matter*, 1(3):113–128, 1998. cond-mat/9810009.

[28] S. Miller and S. Luding. Event driven simulations in parallel. *J. Comp. Phys.*, 92?:???, 2003.

[29] S. Miller and S. Luding. Cluster growth in two- and three-dimensional granular gases. *Phys. Rev. E*, ???:???, 2004.

[30] B. D. Lubachevsky. Simulating billiards: Serially and in parallel. *Int.J. in Computer Simulation*, 2:373–411, 1992.

[31] S. Luding and A. Goldshtein. Collisional cooling with multi-particle interactions. *Granular Matter*, 5(3):???, 2003.

[32] S. Luding, M. Huthmann, S. McNamara, and A. Zippelius. Homogeneous cooling of rough dissipative particles: Theory and simulations. *Phys. Rev. E*, 58:3416–3425, 1998.

[33] R. Cafiero O. Herbst and S. Luding. A mean field theory for a driven dissipative gas of frictional particles. preprint, 2001.

[34] S. Luding and H. J. Herrmann. Cluster growth in freely cooling granular media. *Chaos*, 9(3):673–681, 1999.

[35] P. K. Haff. Grain flow as a fluid-mechanical phenomenon. *J. Fluid Mech.*, 134:401–430, 1983.

[36] J. T. Jenkins and M. W. Richman. Kinetic theory for plane shear flows of a dense gas of identical, rough, inelastic, circular disks. *Phys. of Fluids*, 28:3485–3494, 1985.

[37] S. McNamara and W. R. Young. Inelastic collapse in two dimensions. *Phys. Rev. E*, 50(1):R28–R31, 1994.

[38] S. Luding, E. Clément, J. Rajchenbach, and J. Duran. Simulations of pattern formation in vibrated granular media. *Europhys. Lett.*, 36(4):247–252, 1996.

[39] S. Luding. Surface waves and pattern formation in vibrated granular media. In *Powders & Grains 97*, pages 373–376, Amsterdam, 1997. Balkema.

[40] S. Luding, M. Lätzel, W. Volk, S. Diebels, and H. J. Herrmann. From discrete element simulations to a continuum model. *Comp. Meth. Appl. Mech. Engng.*, 191:21–28, 2001.

[41] S. Luding. Liquid-solid transition in bi-disperse granulates. *Advances in Complex Systems*, 4(4):379–388, 2002.

[42] H. Kawamura. A simple theory of hard disk transition. *Prog. Theor. Physics*, 61:1584–1596, 1979.

[43] M. Alam, J. T. Willits, B. O. Arnarson, and S. Luding. Kinetic theory of a binary mixture of nearly elastic disks with size and mass-disparity. *Physics of Fluids*, 14(11):4085–4087, 2002.

[44] M. Alam and S. Luding. How good is the equipartition assumption for transport properties of a granular mixture. *Granular Matter*, 4(3):139–142, 2002.

[45] M. Alam and S. Luding. Rheology of bidisperse granular mixtures via event driven simulations. *J. Fluid Mech.*, 476:69–103, 2003.

[46] M. Alam and S. Luding. First normal stress difference and crystallization in a dense sheared granular fluid. *Phys. Fluids*, 15(8):2298–2312, 2003.

[47] S. Luding and H. J. Herrmann. Micro-macro transition for cohesive granular media. in: Bericht Nr. II-7, Inst. für Mechanik, Universität Stuttgart, S. Diebels (Ed.), 2001.

[48] S. Luding. Micro-macro transition for anisotropic, periodic, elastic solids. in preparation, 2004.

[49] J. Schwedes. Review on testers for measuring flow properties of bulk solids. *Granular Matter*, 5(1):1–45, 2003.

[50] D. Fenistein and M. van Hecke. Kinematics – wide shear zones in granular bulk flow. *Nature*, 425(6955):256, 2003.

[51] D. Fenistein, J. W. van de Meent, and M. van Hecke. Universal and wide shear zones in granular bulk flow. *cond-mat/0310409*, 2003.